Soil moisture impacts on convective margins

BENJAMIN R. LINTNER AND J. DAVID NEELIN

Department of Atmospheric Sciences, and Institute of Geophysics and Planetary Physics, University of California, Los Angeles

(November 28, 2008)

ABSTRACT

An idealized prototype for the location of the margins of tropical land region convection zones is extended to incorporate the effects of soil moisture and associated evaporation. The impact of evaporation, integrated over the inflow trajectory into the convection zone, is realized nonlocally where the atmosphere becomes favorable to deep convection. This integrated effect produces "hotspots" of land surface-atmosphere coupling downstream of soil moisture conditions. Overall, soil moisture increases the variability of the convective margin, although how it does so is nontrivial. In particular, there is an asymmetry in displacements of the convective margin between anomalous inflow and outflow conditions which is absent when soil moisture is not included. Furthermore, the simple cases presented here illustrate how margin sensitivity depends strongly on the interplay of factors including net top-of-the-atmosphere radiative heating, the statistics of inflow wind, and the convective parameterization.

1. Introduction

As transition zones between strong and weak mean precipitation regimes, the margins of tropical land region convection zones experience significant variability. Interannually, some of the most severe droughts occur as localized spatial shifts in the margins of convection zones. Moreover, the tropical hydrologic cycle signatures of greenhouse gas-induced climate change as simulated by models are often strongly localized along particular convective margins, albeit with significant intermodel differences regarding precisely where such changes occur (Williams et al., 2001; Douville et al., 2002; Johns et al., 2003; Soden and Held, 2006; Neelin et al., 2006; IPCC, 2007; Chou et al., 2008).

Given the variability inherent to convective margins, there is a need for detailed mechanistic understanding of the factors controlling their behavior. In previous work, Lintner and Neelin (2007; hereafter LN07) developed a simple prototype to describe convective margins under idealized conditions of low-level dry air inflow into a land region from an adjacent ocean. The LN07 prototype demonstrates how the characteristics of such inflow convective margins, e.g., the location of the transition between nonconvecting and convecting conditions, depend on dynamic and thermodynamic variables, including low-level circulation, inflow moisture, and tropospheric temperature.

For simplicity, the LN07 analysis neglected the effect of land surface conditions such as soil moisture on convective margins and their variability. Of course, the capacity of the land surface to retain moisture significantly influences the climate system. Soil moisture directly impacts surface-atmosphere energy fluxes through evaporation, which modulates the partitioning of the surface energy budget (Charney, 1975; Shukla and Mintz, 1982; Delworth and Manabe, 1988). Soil moisture further constrains vegetative characteristics, thereby impacting surface parameters like albedo and surface roughness that in turn affect surface radiative properties and turbulent exchanges of energy, moisture, and momentum (Xue and Shukla, 1993). The persistence of soil moisture on seasonal (or longer) timescales provides a source of memory to the climate system (Vinnikov et al., 1996).

Much interest has focused on soil moisture's influence on precipitation and its variability, especially the positive feedback through which anomalous precipitation conditions are self-sustained and amplified by the land surface state. The existence of such feedbacks has implications for predictability and long-range forecast skill, e.g., the two-way interactions between the land surface and atmosphere are thought to play a role in the persistence of drought conditions over land regions (Hong and Kalnay, 2000; d'Odorico and Porporato, 2004). Observational studies based on large-scale irrigation projects (Stidd, 1975; Barnston and Schickedanz, 1984; Moore and Rojstaczer, 2002), soil moisture field measurement networks (Findell and Eltahir, 1997 and 1999), and precipitation persistence statistics (Taylor et al., 1997; Taylor and Lebel, 1998; Taylor et al., 2003; Koster and Suarez, 2004) point to the operation of the soil moisture-precipitation feedback in nature. General circulation model (GCM) also manifest the soil moisture-precipitation feedback (Atlas et al., 1993; Beljaars et al., 1996; Zheng and Eltahir, 1998; Pal and Eltahir, 2001, 2003; D'Odorico and Porporato, 2004), although fundamental questions remain regarding the feedback's magnitude and sensitivity to model parameterizations (Koster et al., 2004; Dirmeyer et al., 2006; Wu et al., 2007; Steiner et al., 2008).

One feature of the soil moisture-precipitation feedback that has emerged from recent model studies is the occurrence of localized regions– "hotspots"–of strong land surface-atmosphere coupling (Koster et al., 2004; Guo et al., 2006; Notaro, 2008). Within the Tropics, such hotspots typically appear in the transition zones between the wettest and driest mean climates. Koster et al., (2004) stressed the role of soil moisture in producing the locally intensified soil moisture-precipitation coupling. Within the driest regions, evaporation exhibits significant sensitivity to soil moisture but overall evaporative rates are small, with limited potential to affect precipitation. Within the wettest regions, soil moisture perturbations cause only small variations in evaporation, since the sensitivity of evaporation to soil moisture diminishes as the surface approaches saturation. It is somewhere between the wettest and driest extremes that soil moisture perturbations are most conducive to driving variations in precipitation.

Although the role of atmospheric dynamics and convection is inherent in this view of hotspots, the focus of the present study is to elucidate the atmospheric side of land-atmosphere coupling. In particular, we consider circumstances under which the large-scale inflow air mass characteristics into a land region convection zone modulate precipitation along the convective margin, with an emphasis on diagnosing the interplay of margin variability and the underlying surface conditions. Since our principal objective is to develop basic insights into soil moisture influences on convective margin variability, we develop analytic prototypes to illustrate mechanisms. We also employ an intermediate level complexity model coupled to a simplified land surface scheme. What this model lacks in terms of realism is leveraged against the ease with which it can be analyzed and interpreted, although even the simple cases considered manifest nontrivial behavior. We further explore the extent to which the results of this analysis may be applied to the analysis of more complex models as well as the observations.

2. Soil moisture impact inferred from an intermediate level complexity model

The model used is the Quasi-equilibrium Tropical Circulation Model 1 Version 2.3 (QTCM1; Neelin and Zeng, 2000; Zeng et al., 2000), an intermediate level complexity model of the tropical troposphere. An advantage of QTCM1 over conventional GCMs is the simplicity of the model framework: QTCM1's relative transparency facilitates diagnosis in ways that are not always feasible or straightforward with GCMs. The simplicity of QTCM1 has rendered it a useful interpretive tool in elucidating many tropical climate phenomena, including tropical ocean-atmosphere coupling (Su et al., 2003), El Niño/Southern Oscillation (ENSO) tropical teleconnections (Neelin and Su, 2005), climate sensitivity to global warming (Chou and Neelin, 2004), intraseasonal variability (Lin et al., 2000), monsoon climates (Chou and Neelin, 2003), and vegetation-atmosphere interactions (Zeng et al., 1999).

For all QTCM1 simulations considered below, we have implemented a land surface model consisting of a simple bucket formulation, with evaporation E linearly proportional to potential evaporation E_p, i.e., $E = \beta(w)E_p$, where the evaporation efficiency $\beta(w)$ is a function of the soil wetness w. The latter is a dimensionless quantity obtained by normalizing the soil moisture content by the holding capacity w_0; w ranges between 0 and 1, with w = 0 (= 1) representing a completely dessicated (saturated) surface, although w effectively maximizes at values < 1 because of constraints imposed by atmospheric thermodynamics. In our implementation, $\beta(w) = w$ and $w_0 = 150$ mm unless otherwise stated. The total surface runoff is modeled as $w^4 P$, where P is precipitation. Although this bucket model formulation neglects many of the features necessary to provide a fully realistic picture of land-atmosphere coupling, it is sufficient for illustrating the mechanisms examined here.

We consider first a set of experiments motivated by approaches to investigate soil moisture impacts in prior studies (e.g., Koster et al., 2004). In particular, we performed a control simulation (CTL) and a sensitivity simulation in which $\beta(w)$ was fixed to a climatology that produces the same mean evaporation as CTL, i.e., $\beta(w)^* = [\overline{\beta(w)} + \overline{\beta(w)' E_p'}/\overline{E_p}]_{CTL}$ ("fixed β"). Here, overbars and primes denote time-means and deviations from time-means, respectively. Each simulation was forced with imposed climatological monthly-mean sea surface temperatures (SSTs), such that the variability present arises solely from QTCM1's internal dynamics. The simulations were performed at a horizontal resolution of 1.40625° x 1°, with output saved as 5-day (pentadal) means for 25 years.

The standard deviations of 3-month seasonal mean precipitation values for tropical South America in the CTL simulation (σ_{CTL}) indicate the largest variability occurring not at the highest mean precipitation rates (here > 14 mm day^{-1}) but rather at somewhat lower values (4 - 10 mm day^{-1}), i.e., along the margins of strong seasonal convection zones (Figure 1a). A convective margin of the type considered by LN07, i.e., low-level inflow from an adjacent ocean region into a land region, occurs in northeastern South America during boreal autumn (September-November). An important caveat here is that QTCM1, like many models, exaggerates the relative importance of convective margin variability, since the model simulates too little high-frequency variability in the interior of the convection zone (Lin et al., 2000).

The ratio of σ_{CTL} to $\sigma_{\beta(w)^*}$ provides a measure of the importance of interactive soil moisture variations to total precipitation variability in QTCM1 (Figure 1b; shaded contours). Generally, the largest increases of precipitation variability by soil moisture are localized to the convective margins, although there is sizable spatial variation in the effect. The geographic distribution of the interactive soil moisture amplification of precipitation variability over tropical South America is broadly consistent with the pattern of soil moisture-precipitation coupling hotspots evident in prior studies (c.f., Figure 1 of Koster et al., 2004 for a comparison to JJA). Other regions of substantial soil moisture-precipitation coupling in QTCM1 include the Sahel region of Africa and northern Australia (not shown). QTCM1's ability to simulate hotspots means that the model has some utility in diagnosing hotspot genesis, a topic to which we return later. In the following section, we employ an analytic prototype to address modifications to convective margin behavior in the presence of soil moisture and evaporation.

3. Incorporating evaporation into the convective margins framework

a. Set-up

The vertically-averaged tropospheric temperature and moisture equations, as defined in LN07, but with the addition of evaporation and an explicit surface energy constraint, are:

$$M_s \nabla \cdot \mathbf{v} = P + R_{surf} + R_{toa} + H \qquad (1)$$

$$-(M_{qp} q) \nabla \cdot \mathbf{v} = -u_q \partial_x q + E - P \qquad (2)$$

$$R_{surf} + E + H = 0 \qquad (3)$$

where R_{surf} and R_{toa} are, respectively, the net surface and top-of-the-atmosphere shortwave plus longwave radiative heating; E is evaporation (or evapotranspiration); H is sensible heat flux; P precipitation, i.e., convecting heating in (1) or drying in (2); u_q is the projection of the windfield onto the vertical structure of moisture, and M_s and $M_q = M_{qp} q$ are dry static stability and moisture stratification, respectively. Adding (1) and (2) and invoking the constraint (3) yields an expression for the horizontal convergence, i.e.,

$$\nabla \cdot \mathbf{v} = M^{-1}[R_{toa} - u_q \partial_x q] \qquad (4)$$

which upon substitution into the moisture equation (2) yields:

$$P = E - u_q \partial_x q(1 + M_{qp} q/M) + M_{qp} q R_{toa}/M \qquad (5)$$

Here, $M = M_s - M_{qp} q$ denotes the gross moist stability.

For nonconvecting regions, with $P = 0$, it is instructive to consider instead

$$\nabla \cdot \mathbf{v}_{nc} = M_s^{-1}[R_{toa} - E] \qquad (6)$$

The nonconvecting region moisture equation is then:

$$u_q \partial_x q = M_{qp} q {M_s}^{-1}[R_{toa} - E] + E \qquad (7)$$

From (7), it can be seen that E has two effects that tend to cancel. On the one hand, $E > 0$ corresponds to a source of tropospheric moisture, while on the other, $E > 0$ offsets the effect of net energy input at the top of the atmosphere ($R_{toa} > 0$), reducing $\nabla \cdot \mathbf{v}_{nc}$. Combining the terms in E shows the effective contribution of E is scaled by a factor of $(1 - M_{qp} q {M_s}^{-1}) = M {M_s}^{-1}$.

For the idealized steady-state convective margin solution of LN07, E in the nonconvecting portion of the domain was set to zero, since $w = 0$ in the absence of recharge by precipitation. However, realistic situations for which E is nonzero are encountered on seasonal or subseasonal timescales, as with the annual cycle movements of land region convection zones, since the decay time for w is of order a few months.

b. Shift of the convective margin associated with an imposed evaporation in the nonconvecting region

It is notationally convenient to recast (7) as

$$\partial_x q - \lambda_E(x) q = u_q^{-1} E \qquad (8)$$

where

$$\lambda_E(x) = M_{qp}(M_s u_q)^{-1}[R_{toa} - E] \qquad (9)$$

$\lambda_E(x)$, which is in units of length^{-1}, can be interpreted as the local spatial rate of moisture increase along an inflow trajectory associated with moisture convergence.

For arbitrary $R_{toa}(x)$ and $E(x)$, integrating (8) between the inflow position (at x_0) and x yields:

$$q(x) = e^{\Lambda(x)}[q(x_0) + \int_{x_0}^{x} e^{-\Lambda(x')} u_q^{-1} E(x') dx'] \qquad (10)$$

where $\Lambda(x) = \int_{x_0}^{x} \lambda_E(x')dx'$. The second term in brackets on the right-hand side of (10) represents the spatially-integrated effect of evaporation across the nonconvecting region. For illustrative purposes, taking $R_{toa}(x)$ and $E(x)$ as constants in the nonconvecting region, (10) yields (setting x_0 = 0),

$$q(x) = (q_0 + q_E)e^{\lambda_E x} - q_E \qquad (11)$$

where q_0 is the inflow specific humidity and $q_E = (u_q \lambda_E)^{-1}E = M_s E/M_{qp}(R_{toa} - E)$ is a moisture scale associated with evaporation and convergence. If $E > R_{toa}$, leading to divergence in (6), the moisture scale associated with q_E (with sign reversed) represents the value of moisture for which evaporation and moisture divergence balance, with the inflow q_0 decaying toward it. On the other hand, under conditions with $E < R_{toa}$, moisture increases exponentially along the inflow trajectory. We point out that q_E increases moisture along the inflow trajectory; however, λ_E is smaller, relative to no-evaporation conditions, which reduces q. This behavior reflects the compensation between moistening directly associated with E and lowered convergence indirectly associated with changes to column flux forcing.

For a temperature-dependent convective threshold condition in moisture $q_c(T)$, the convective margin occurs at:

$$x_c^E = \lambda_E^{-1} \ln[(q_c(T) + q_E)/(q_0 + q_E)] \qquad (12)$$

As illustrated in Figure 2a, for a given R_{toa}, x_c^E decreases as E increases, i.e., the margin shifts closer to the inflow point. The displacement of the margin toward the inflow point implies that the direct moistening effect of E in q_E dominates over the reduction of convergence in λ_E. In terms of the dependence of (12) on top-of-the-atmosphere radiative heating, as R_{toa} is increased, x_c^E moves closer to the inflow point, since larger R_{toa} enhances vertical moisture convergence. Further, Figure 2b show stronger sensitivity of x_c^E to the inclusion of evaporation with E small, with larger sensitivity of x_c^E to E perturbations for a specified value of E when R_{toa} is small. Note that while the value of q_E becomes large as $R_{toa} \to E$, the value of x_c becomes large as $R_{toa} \to -M_{q_c} M_s^{-1} E$, where $M_{q_c} = M_{qp} q_c(T)$.

Based on these results, convective margin sensitivity to E in models or observations should be strongly affected by the relative values of R_{toa} and E. Moving poleward from the Tropics, R_{toa} varies as a result of the latitudinal variation in top-of-the-atmosphere insolation; in the winter hemisphere, or during the equinoctal seasons, the meridional decrease of top-of-the-atmosphere insolation causes R_{toa} to become small and, at some latitude, to change sign. (Such latitude dependence is roughly analogous to the x-axis in Figure 2a.) With the caveats that (12) strictly applies to steady-state conditions and simplified inflow geometries, increased margin sensitivity is anticipated to occur at particular locations dictated by the interplay of the various control factors.

c. *Asymmetric displacements of the convective margin under anomalous windfield perturbations*

Having considered the shift in x_c that occurs with inclusion of evaporation, we now discuss the related issue of margin variations to imposed windfield perturbations δu_q in the presence of nonzero E. The starting point is the mean state of LN07, with $E(x) = 0$ outside of the convecting region ($x < x_c^0$) and $E(x) = E$ inside ($x > x_c^0$).

For anomalous outflow ($\delta u_q < 0$), the low-level wind perturbation induces the margin to move toward the inflow point, over a dry surface. The solution is thus identical to LN07, but with $u_q \to u_q + \delta u_q$; thus,

$$\delta x_c = (\delta u_q/u_q)\lambda_0^{-1} \ln(q_c/q_0) \qquad \text{[outflow]} \qquad (13)$$

For anomalous inflow ($\delta u_q > 0$), by contrast, the margin will be shifted away from the inflow point, over a residually wet surface. From (10), it can be shown that

$$\delta x_c = (1+\delta u_q/u_q)\lambda_E^{-1} \ln[\frac{1 + q_E/q_c}{(q_0/q_c)^{\delta u_q/(u_q+\delta u_q)} + q_E/q_c}] \qquad \text{[inflow]} \qquad (14)$$

In the limit $\delta u_q/u_q \to 0$, (14) is, to first order in $\delta u_q/u_q$,

$$\delta x_c \approx x_c^0(\delta u_q/u_q)\frac{1}{1 + (M_s - M_{q_c})E/(M_{q_c}R_{toa})} \qquad \text{[inflow]} \qquad (15)$$

Equation (15) looks like (13), but modified by a factor of $\kappa = [1 + (M_s - M_{q_c})E/(M_{q_c}R_{toa})]^{-1}$. Since all terms in κ are positive, $\kappa < 1$, which means that for δu_q of given magnitude, the x_c displacements for anomalous inflow conditions are smaller than for anomalous outflow conditions. Such asymmetric displacements arise from the distinct surface states encountered under inflow and outflow perturbations: with the former air masses approaching the convective margin interact with a wet surface near the margin, which enhances the moisture loading of the inflow relative to what it would be upon transiting over a dry surface. The residual moistening allows q_c to be met earlier along the inflow trajectory. For typical (QTCM1) values of E, R_{toa}, M_{q_c}, and M, $\kappa \approx$ 0.5-0.75.

d. *Timescale for margin adjustment*

The prototype effectively assumes time-independent surface states; in reality, the surface adjusts to the margin displacement, e.g., the initially wet surface encountered under anomalous inflow conditions will begin to dry as evaporative demand diminishes soil wetness. The timescale for margin adjustments, τ_{margin}, is approximately $\delta x_c/u_q \approx (\delta u_q/u_q)\frac{M_s \ln(q_c(T)/q_0)}{M_{qp}(R-E)}$, which is of order $30(\delta u_q/u_q)$ days for the configuration discussed in the next section. On the other hand, the evaporative timescale, τ_E, is approximately $\frac{L_H w_0}{E_p}$, where L_H is the latent heat of vaporization and potential evaporation is approximately constant. For E_p of order 100 Wm^{-2}, and w_0 =150 mm, $\tau_E \approx 45$ days. For small wind perturbations (i.e., $30(\delta u_q/u_q) << 45$ days), the margin will effectively adjust before the surface state is substantially altered. At lower (e.g., seasonal) frequencies, the surface evolution may play a role, as considered in Section 6. Also, for regions where $R_{toa} \rightarrow E$, τ_{margin} becomes large, so that the atmospheric adjustment timescale may become non-negligible relative to τ_E.

4. Implications of soil moisture for high-frequency variability of the convective margin

a. Idealized QTCM1 configuration

In this section, the results of several idealized QTCM1 simulations designed specifically to provide insights into soil moisture impacts on convective margins are discussed. The model set-up here consists of an equatorial, zonal strip half occupied by a single ocean and land region. For the ocean region, uniform SST was imposed. Top-of-the-atmosphere insolation and surface albedo values were set to mean April conditions at the equator. Also, the tropospheric temperature equation was cast assuming the weak temperature gradient (WTG) approximation, where horizontal T gradients in radiative and turbulent fluxes and temperature advection/diffusion are neglected (Sobel and Bretherton, 2000). In each simulation discussed below, the temperature profile is prescribed to a fixed value.

Under steady state conditions, the idealized QTCM1 tropical strip simulation yields a single convection zone symmetric about the mid-point of the land region. To generate variations in the convection zone, spatially-uniform, Gaussian-distributed stochastic wind perturbations were imposed in the model's moisture advection scheme. For computational and diagnostic simplicity, the perturbations were added to the barotropic component of the total windfield over 10-day intervals. The resulting precipitation profile, averaged over 500 perturbations, appears in Figure 3 (solid red line; hereafter, we refer to this simulation as STND). Note that the x-coordinate shown here is normalized relative to the non-perturbed precipitation profile: $x = 1$ corresponds to the location of x_c in the steady state, defined relative to the land-ocean interface at $x = 0$. The principal impact of the imposed perturbations is a smoothing of the precipitation profile: the imposed perturbations essentially displace the edge of the convection zone back and forth, such that for the mean over a large number of perturbations, a smoothly tapered profile emerges.

b. Fixed β and no-wetness memory experiments

To demonstrate how soil moisture impacts the variability of the convective margin, two sensitivity experiments were conducted. One sensitivity case implemented fixed β conditions, with the β estimated (as in Section 2) from STND. The other used E estimated functionally from P at each land gridpoint through a 6th-order polynomial fit between the mean E and P fields obtained from STND. This "no wetness memory" simulation suppresses residual soil moisture anomalies associated with prior P and is effectively equivalent to taking $w_0 \rightarrow 0$.

Under fixed β conditions, there is little impact on the mean precipitation profile (Figure 3; solid blue line); however, there is a reduction of σ_P (dashed blue line) by up to 20%. For the no wetness memory case, the mean precipitation profile (green line) is lowered in the transition to the strongest precipitation values. The change in mean behavior of this simulation can be understood in the context of the prototype results of Section 3b: by eliminating residual soil moisture outside of the convection zone–and thus any evaporative moistening from the surface–the mean inflow into the convection zone is drier compared to either the STND or fixed β cases, resulting in reduced mean precipitation values near the convective margin. σ_P of the no wetness memory case (dashed green line) is enhanced relative to STND, especially on the strongly-convecting side of the profile.

c. Anomalous inflow/outflow asymmetry

For the no wetness memory case, nonzero evaporation occurs locally during a particular model timestep only if P is nonzero at the same location during that timestep. If P ceases–as, for example, when the windfield perturbation shifts the convective margin–the soil moisture impact (and hence E) is instantaneously removed. Relative to the STND case, a negative (inflow) windfield perturbation of given magnitude results in a greater westward displacement of the margin, since the effect of residual w outside of the convecting region is eliminated. Figure 4a, which displays x_c values bin-averaged by the windfield perturbations, δu_0, underscores this behavior, as the x_c values of the STND (red) lie below the no wetness memory values (green) for δu_0 <0. For fixed β, the x_c values for $\delta u_0 < 0$ also lie below those of the no wetness memory case (blue). However, the scatter in the δu_0-x_c relationship for fixed β is attenuated relative to STND. The change in x_c variability confirms the significance of interactive soil moisture perturbations to determining precisely where the transition from nonconvecting to convecting conditions occurs.

Comparing the idealized QTCM1 results to the analytic prototype of Section 3 demonstrates favorable agreement. Assuming no effect from soil moisture (or evaporation) outside of the convection zone, the analytic solution (black) closely matches the no wetness memory case, although the slope of the predicted δu_0-x_c relationship is a little too steep. This discrepancy is largely attributed to non-leading order spatial structure neglected in the analytic solution, e.g., R_{toa} and M_s are not strictly uniform. When the effect of residual E is included, the analytic slope (gray) is reduced for anomalous inflow conditions, with the value approximately matching the fixed β (or STND) results.

As was noted in Section 3b, the value of R_{toa} can affect the sensitivity of the convective margin. Repeating the STND, fixed β, and no wetness memory simulations with R_{toa} reduced (by lowing net top-of-the-atmosphere insolation) underscores this sensitivity (Figure 4b). Much of the increased scatter in the δu_0-x_c relationship (as evidenced by the larger standard errors) is associated with a lengthening of τ_{margin} owing to the reduced convergence. However, despite the increased variability, the anomalous inflow/outflow asymmetry again emerges. The analytic results suggest an increase in the separation of slopes in the absence and presence of residual moisture. However, the mismatch between the analytic solutions and simulated data is much larger in the reduced R_{toa} case, which likely reflects both a greater sensitivity to the spatial structure of the fields and the longer atmospheric adjustment.

5. Diagnostic interpretation of convective margin variability

The diagnostic discussed in this section, the precipitation variance budget, represents one that can be readily estimated from GCM outputs and is therefore a useful metric for model intercomparison. Approaches based on budgetary constraints have gained widespread use in studies of tropical precipitation: example applications include mechanistic analysis of the ENSO tropical teleconnection (Lintner and Chiang, 2005; Neelin and Su, 2005) and attribution of global warming impacts (Chou and Neelin, 2004). Many studies of land surface-atmosphere coupling have also employed budgetary analyses, especially the connection between evaporation and precipitation variances as inferred from soil moisture balance (Budyko, 1974; Brubaker et al., 1993; Koster et al., 2000, 2001; Wu et al., 2007). Here, we consider a budgetary decomposition of precipitation variance from the atmospheric side in order to highlight more explicitly the role of atmospheric processes in the generation of hotspots. Of course, while budgets can provide powerful insights into underlying mechanisms, it may be challenging to tease apart (direct) causal agents from (indirect) feedback processes, e.g., the magnitude of a budget term does not necessarily indicate causality. As will be seen, interpretation of the precipitation variance budget is not completely straightforward even for the idealized set-up considered here; however, viewing the budget in conjunction with margin variations proves instructive.

From the moisture equation (2), the precipitation variance budget is:

$$\sigma_P^2 = \sigma_E^2 + \sigma^2_{-u_q\partial_x q} + \sigma^2_{M_{qp}q\nabla\cdot\mathbf{v}} + 2cov(E, -u_q\partial_x q) + 2cov(E, M_{qp}q\nabla\cdot\mathbf{v}) + 2cov(-u_q\partial_x q, M_{qp}q\nabla\cdot\mathbf{v}) \quad (16)$$

Here, σ_A^2 denotes the variance of A, defined as $\sigma_A^2 = (N^2 - N)^{-1}\Sigma(A_i - < A >)^2$, where $< A >$ is the average of A. Similarly, $cov(A, B)$ denotes the covariance of A and B, $cov(A, B) = (N^2 - N)^{-1}\Sigma(A_i - < A >)(B_i - < B >)$. We emphasize that, for the idealized simulations analyzed here, the perturbative forcing is explicitly prescribed and is thus known *a priori*.

a. *Moisture convergence and advection*

Longitudinal profiles of the terms in (16) for the STND and fixed β simulations (Figures 5a and 5b) demonstrate that the variance associated with moisture convergence, $\sigma^2_{M_{qp}q\nabla\cdot\mathbf{v}}$ (orange line), is typically the largest term. The dominance of moisture convergence is especially evident on the strongly-convecting side of the profile where $\sigma^2_{M_{qp}q\nabla\cdot\mathbf{v}}$ constitutes up to 90% of σ_P^2 (black line). On the other hand, the variance associated with horizontal moisture advection, $\sigma^2_{-u_q\partial_x q}$ (red line), contributes little to the total precipitation variance.

At first glance, the small variance contribution by horizontal moisture advection may appear counterintuitive: after all, it is through moisture advection that the perturbation forcing is imposed in the model. However, the apparent smallness of $\sigma^2_{-u_q\partial_x q}$ relative to σ_P^2 can be reconciled with the expectation that it should be larger by using the relationship (4) to expand the variance of moisture convergence:

$$\sigma^2_{M_{qp}q\nabla\cdot\mathbf{v}} \approx \overline{\gamma}^2\sigma^2_{R_{toa}} + \overline{\gamma}^2\sigma^2_{-u_q\partial_x q} + 2\overline{\gamma}^2 cov(R_{toa}, -u_q\partial_x q) \quad (17)$$

where $\gamma = M_{qp}q/M$. Although fluctuations in γ contribute to $\sigma^2_{M_{qp}q\nabla\cdot\mathbf{v}}$, their impact was observed to be sufficiently small to warrant their neglect in expression (17). The decomposition of moisture convergence reveals that $u_q\partial_x q$ is the dominant contribution to $\sigma^2_{M_{qp}q\nabla\cdot\mathbf{v}}$ (Figure 5c); thus, moisture advection does significantly contribute to σ^2_P, albeit indirectly.

Like moisture convergence, moisture advection can be partitioned according to its definition, i.e.,

$$\sigma^2_{u_q\partial_x q} = (\partial_x\overline{q})^2\sigma^2_{u_q} + \overline{u}_q^2\sigma^2_{\partial_x q} + 2\overline{u}_q\partial_x\overline{q} cov(u_q, \partial_x q) + \mathcal{R}_{adv} \quad (18)$$

where $\mathcal{R}_{adv}$ is a residual consisting of higher-order terms, $\mathcal{R}_{adv} = \Sigma[u'_q\partial_x q' - < u'_q\partial_x q' >][2(\overline{u}_p\partial_x q' + \overline{\partial_x q}u'_q) + (u'_q\partial_x q' - < u'_q\partial_x q' >)]$. The largest contribution to $\sigma^2_{u_q\partial_x q}$ arises from $\overline{u}_q\sigma^2_{\partial_x q}$. Loosely speaking, as the precipitation profile shifts under u_q variations, the steepest portion of the humidity profile (which occurs on the weakly-convecting side of the margin) is displaced, inducing large variations in q and its horizontal gradient.

b. *Evaporation*

Of all terms appearing in (16), the variance associated with evaporation, σ^2_E, manifests the largest difference between the STND and fixed β cases. In the absence of interactive soil moisture perturbations, the contribution of E to P variance is small everywhere. By contrast, for the STND simulation, the evaporative contribution approaches and even slightly exceeds the contribution from moisture convergence at low mean P.

σ^2_E can be decomposed through its definition:

$$\sigma^2_E = \overline{E}_p^2\sigma^2_\beta + \overline{\beta}^2\sigma^2_{E_p} + 2\overline{\beta}\overline{E}_p cov(\beta, E_p) + \mathcal{R}_E \quad (19)$$

where $\mathcal{R}_E$ is a residual defined analogously to $\mathcal{R}_{adv}$, $\mathcal{R}_E = \Sigma[\beta' E'_p - < \beta' E'_p >][2(\overline{E}_p\beta' + \overline{\beta}E'_p) + (\beta' E'_p - < \beta' E'_p >)]$. Averaging the terms in the expansion (19) over x-values close to the maximum of σ^2_E reveals rather nontrivial behavior (Table 1): while $\overline{E}_p^2\sigma^2_\beta$ is the largest term, it is largely balanced by the covariance between β and E_p. The negative covariation of β' and E'_p can be understood as follows. For an anomalously wet surface ($\beta' > 0$), surface temperature (T_s) decreases. The cooler surface is associated with a lowered saturation specific humidity, which yields negative E'_p, since $E_p \propto q^{sat}_{surf}(T_s) - q_{surf}$. For fixed β, on the other hand, only the variance associated with E_p is nonzero (since $\beta' = 0$), but the magnitude of this term (0.2 mm^2 day^{-2}) is considerably reduced relative to its value in STND (9.6 mm^2 day^{-2}). This behavior illustrates a cautionary aspect of budgetary approaches, namely that they may obfuscate underlying physical mechanisms through covariances and compensation between terms.

The peak value of σ^2_E/σ^2_P in the STND case, 0.4, coincides with a mean P of approximately 2 mm day^{-1}, which is consistent with localization of the strongest soil moisture-precipitation coupling between extreme convection regimes. (For $P < 2$ mm day^{-1}, $cov(E, M_{qp}q\nabla\cdot\mathbf{v})$ dominates σ^2_p.) Considering the variance differences between the STND and fixed β simulations further highlights the importance of interactive soil moisture to σ^2_P (Figure 6a). Note that the variance differences have been plotted as a function of mean precipitation, which in the simplified set-up here is effectively a monotonic function of the distance from the edge of the convection zone. For $P < 4$ mm day^{-1}, the difference in σ^2_E ($\Delta\sigma^2_E$) can account for all of the difference in σ^2_P ($\Delta\sigma^2_P$) between the two simulations; in fact, since $\Delta\sigma^2_E > \Delta\sigma^2_P$ for low mean P, the difference in the sum of remaining variance terms is negative. On the other hand, at high mean P, $\Delta\sigma^2_P$ is accounted for by remaining terms (which include covariances with E).

One interpretation of the behavior in Figure 6a is that $\Delta\sigma^2_P - \Delta\sigma^2_E$ represents a downstream, nonlocal feedback to soil moisture perturbations. In this view, a substantial portion of the precipitation change is realized downstream of where the E contribution to P variance is maximized, i.e., at larger mean P values, where $\sigma^2_{M_{qp}q\nabla\cdot\mathbf{v}}$ dominates σ^2_p. Thus, the the P changes associated with interactive β occur over a larger range of mean P values (or, equivalently, a larger spatial scale) than do the evaporative changes themselves. The nonlocality implied by $\Delta\sigma^2_P - \Delta\sigma^2_E$ is qualitatively consistent with the analysis of Schär et al., (1999), which stressed the role of horizontal advection (and nonlocality) to soil moisture-precipitation coupling.

c. *Effect of changes to the convective parameterization*

We also briefly comment on the effect of simulation physics–specifically, the convective parameterization–in determining the degree of locality manifested in the soil moisture-precipitation coupling. Convective parameterizations represent a significant source of divergence among current generation climate models, and a wide range of simulated quantities are known to be sensitive to the details of convective parameterizations (Zhang and McFarlane, 1995; Maloney and Hartmann, 2001; Gochis et al., 2002; Knutson and Tuleya, 2004). To illustrate how convective parameterizations may affect land surface-atmosphere coupling, we performed two additional sets of idealized QTCM1 simulations with lower and higher values of the convective adjustment timescale (τ_c) in the model's Betts and Miller (1986) convection scheme. The principal impact of decreasing (increasing) τ_c is a steepening (flattening) of the mean edge of the convection zone. Decreasing τ_c further increases precipitation variability under u_q perturbations.

In terms of the variance differences between interactive and fixed β cases, alterations to τ_c have a demonstrable impact. Overall, the values of $\Delta\sigma_P^2$ and $\Delta\sigma_E^2$ increase as τ_c decreases (Figure 6b). However, the contribution of $\Delta\sigma_E^2$ to $\Delta\sigma_P^2$ is seen to decrease as τ_c is reduced, while the peak of $\Delta\sigma_P^2$ is shifted deeper into the convection zone (toward higher mean P). These features suggest an increase of the downstream, nonlocal contributions to $\Delta\sigma_P^2$ as τ_c is reduced. A broader implication of such behavior is that the characteristics of land-atmosphere coupling in models–e.g., the degree of "hotspotedness" expressed by a model–can be impacted by model configuration.

6. Example of the soil moisture effect on precipitation seasonality

Over an annual cycle, the location of peak tropical convection varies latitudinally with changes in net top-of-the-atmosphere radiative heating. Other factors may substantially modulate the meridional location of peak convection. In the case of monsoon systems, for example, local land-ocean thermal contrasts may exert a leading-order influence on the intensity and duration of monsoonal rainfall (e.g., Steiner et al., 2008). Apart from the meridional seasonality of tropical precipitation, some zonal seasonality is also evident: for tropical South America, the eastern equatorial Amazon experiences its driest conditions during austral spring (Wang and Fu, 2002). Such seasonality is driven both by local land-ocean thermal contrasts and interactions of convection with large-scale circulation.

The inflow-evaporative moistening asymmetry described in Sections 3 and 4 may potentially contribute to land region seasonality, which we briefly explore here. We limit focus to the seasonal cycle of P at 5°S over the northeastern corner of South America as simulated by QTCM1 configured with realistic geometry, as in Section 2. The choice of region is motivated by the straightforward applicability of the LN07 prototype to the convective margin behavior here. Specifically, the circulation geometry is relatively simple, consisting of mostly zonal trade wind inflow from the equatorial Atlantic.

a. *Impact of changing soil moisture holding capacity*

In order to estimate soil moisture impacts on the convective margin at 5°S, we consider two experiments in which w_0 is set to either 150 mm or 15 mm. Varying w_0 in this way may be viewed as altering one or more of the physical characteristics of the surface, such as vegetation type and fraction of bare soil. A value of 15 mm approximates a bare, "deforested" surface for which the soil moisture holding capacity is severely restricted.

The convective margin as simulated by QTCM1 for w_0 =150 mm displays a pronounced seasonal cycle (Figure 7, black line). From January through July, the convective edge at 5°S lies near or to the east of the land-ocean interface. At the beginning of August, the margin recedes sharply westward, approaching roughly 50°W, or 1300 km from the Atlantic coastline, by the beginning of September. Thereafter, the margin advances eastward through the end of the year. To leading order, such seasonality is consistent with the seasonal evolution SSTs in the neighboring tropical Atlantic, which are coolest when the margin is at its maximum westward position. In the context of the margins prototype, the cool ocean surface is associated with low q_0, which (for other factors being more-or-less equal) results in x_c occurring relatively far to the west of the Atlantic coast.

The net impact of reducing w_0 to 15 mm induces a westward shift of the margin of up to 2° relative to the simulation with larger w_0 =150 mm. As the margin recedes westward from the land-ocean interface, the surface in the nonconvecting region between the coastal inflow point and x_c begins to dry. Since the w_0 = 15 mm surface has a smaller moisture reservoir than the w_0 = 150 mm case, it dries more rapidly once the westward margin recession begins. Thus, the surface in the w_0 = 15 mm case is relatively drier as the margin retreats inland, so the inflowing air must experience further vertical convergence-induced moistening to achieve the q_c threshold, resulting in an overall lengthening of the distance to reach the margin.

b. *Explicit removal of residual soil moisture outside of the convection zone*

To this point, we have not distinguished between the effect of soil moisture outside of the convection zone (i.e., between the Atlantic coast and x_c) relative to the soil moisture inside. While the interaction with inflow described in previous sections requires outside soil moisture, interactive soil moisture inside of the convection zone could also potentially contribute. For example, local evaporative recycling increases precipitation, which in turn induces cloud-radiative effects that may alter the temperature profile in the vicinity of the margin, thus affecting $q_c(T)$. To demonstrate conclusively that it is the soil moisture outside the margin that matters most here, we performed an additional simulation, this time removing the soil moisture completely from the outer region once the margin has retreated. Figure 8 illustrates cross-sections of precipitation, evaporation, and soil wetness at 5°S for this simulation as well as the standard set-up (in gray and black, respectively), averaged over pentads 50-54. Comparison of the two precipitation profiles indicates a pronounced shift of the margin, by some 2-3°, which illustrates the impact of soil moisture outside of the convection zone.

7. Summary and conclusions

We considered here the impacts of soil moisture on precipitation from the perspective of tropical land region convective margins. The straightforward extension of the LN07 convective margins prototype to include the effects of soil moisture acting through evaporation provides some basic intuition about how surface conditions modulate the transition from nonconvecting to convecting conditions over tropical land regions. For the case of low-level inflow into a convection zone, the integrated effect of evaporation along the inflow trajectory moistens air masses approaching the margin; relative to a comparable trajectory over a dry surface, the moisture tends to increase more rapidly along the inflow path, as expected. Given a moisture threshold condition for deep convection to occur, the integrated evaporation effect induces a shift of the convective margin toward the initial inflow location. This shift depends on E as well as factors determining the large-scale convergence along the trajectory, notably the top-of-the-atmosphere radiative heating R_{toa}. In fact, E lowers the large-scale convergence, but for realistic parameters, the direct evaporative moistening dominates over the convergence reduction.

The analytic prototype also demonstrates how the land surface can affect the variability of the convective margin. In particular, it was shown under inflow wind perturbations, inclusion of E yields an asymmetry in the margin displacements: under conditions of stronger low-level flow into the convection zone (anomalous inflow), marginal displacements are smaller than those for anomalous outflow conditions of the same magnitude. The reason for such asymmetry is that, under anomalous inflow, the margin moves over a residually wet surface, which moistens the inflow into the convective region and allows the convective threshold to be met sooner than it would otherwise. Idealized experiments with an intermediate level complexity model, QTCM1, coupled to a simplified land surface scheme in which soil moisture memory is artificially suppressed do not show this asymmetry. While the magnitude of the asymmetry as suggested by QTCM1 simulations under more realistic conditions (e.g., a longitudinal shift of 2-3° for the set-up in Figure 8) appears modest, it may nevertheless be relevant to the interpretation of the characteristics of tropical land region precipitation seasonality, such as the timing and spatial extent of marginal advances and retreats.

Within QTCM1, we also observed behavior reminiscent of the hotspots of strong soil moisture-convective coupling seen in previous studies such as Koster et al., (2004). Comparison of simulations with and without interactive soil moisture suggested amplification of precipitation variability via soil moisture by ∼20% in the vicinity of the convective margin. The spatial colocation of the peak soil moisture-driven precipitation variability increase with convective margins is a fairly robust characteristic of simulated hotspots. We used an idealized tropical strip QTCM1 configuration to generate hotspots along the margin of the convection zone by imposed perturbations to horizontal moisture advection. It is worth noting that, even in the idealized cases considered here, analysis of precipitation variance budgets proved challenging because of the multiple terms involved, although the mechanistic understanding of convective margins facilitates interpretation of budget behavior. An aspect of the budget analysis of particular note is the nonlocality of soil moisture impacts, with a significant portion of the precipitation response occurring downstream of where soil moisture (and evaporation) is most variable.

Alteration of the model's convection scheme, specifically the timescale for convective adjustment, further demonstrates how the characteristics of hotspots may be affected by model representation of atmospheric processes. Other "atmospheric-side" factors that may affect hotspot characteristics, based on this prototype, include top-of-the-atmosphere heating and large-scale convergence; the mean and variance of inflow wind; and the convective moisture threshold. These factors interact nonlinearly in setting the convective margin, and they may generate substantial regional variation in margin sensitivity to perturbations. Together, they provide an indication of why the strength of simulated land-atmosphere coupling may vary among models.

Acknowledgments. The authors thank R. D. Koster and N. Zeng for insightful discussion and J. E. Meyerson for graphical assistance. This work was supported partly by National Oceanic and Atmospheric Administration NA08OAR4310882 and NA08OAR4310597 and National Science Foundation ATM-0645200. JDN acknowledges sabbatical support from the J. S. Guggen-

heim Memorial Foundation.

REFERENCES

Atlas, R., N. Wolfson, and J. Terry, 1993: The effect of SST and soil-moisture anomalies on GLA model simulations of the 1988 U.S. summer drought. *J. Climate*, **6**, 2034–2048.

Barnston, A.G., and P.T. Schickedanz, 1984: The effect of irrigation on warm season precipitation in the southern Great Plains. *J. Clim. Appl. Meteor.*, **23**, 865–888.

Beljaars, A.C.M., P. Viterbo, M.J. Miller, and A.K. Betts, 1996: The anomalous rainfall over the United States during July, 1993: Sensitivity to land surface parameterization and soil moisture anomalies. *Mon. Wea. Rev.*, **124**, 362–383.

Betts, A. K., and M. J. Miller, 1986: A new convective adjustment scheme. 2. Single column model tests using GATE Wave, BOMEX, ATEX, and arctic air-mass data sets. *Quart. J. Roy. Meteor. Soc.*, **112**, 693–709.

Brubaker, K.L., D. Entekhabi, and P.S. Eagleson, 1993: Estimation of continental precipitation recycling. *J. Climate*, **6**, 1077–1089.

Budyko, M.I., 1974: *Climate and Life*, 508 pp., Academic Press, New York.

Charney, J. G., 1975: Dynamics of deserts and drought in the Sahel. *Quart. J. Roy. Meteor. Soc.*, **101**, 193–202.

Chou, C., and J.D. Neelin, 2003: Mechanisms limiting the northward extent of the northern summer monsoons over North America, Asia, and Africa. *J. Climate*, **16**, 406–425.

Chou, C., and J.D. Neelin, 2004: Mechanisms of global warming impacts on regional tropical precipitation. *J. Climate*, **17**, 2688–2701.

Chou, C., J.D. Neelin, C.-A. Chen, and J.-Y. Tu, 2008: Evaluating the "rich-get-richer" mechanism in tropical precipitation change under global warming. *Submitted to J. Clim.*

Delworth, T.L., and S. Manabe, 1988: The influence of potential evaporation on the variabilies of simulated soil wetness and climate. *J. Climate*, **1**, 523–547.

Dirmeyer, P.A., R.D. Koster, and Z.C. Guo, 2006: Do global models properly represent the feedback between land and atmosphere? *J. Hydrometeor.*, **7** (6), 1177–1198.

D'Odorico, P., and A. Porporato, 2004: Preferential states in soil moisture and climate dynamics. *Proc. Nat. Aca. Sci.* **101** (24), 8848–8851.

Douville H., F. Chauvin, S. Planton, J.F. Royer, D. Salas-Melia, S. Tyteca, 2002: Sensitivity of the hydrological cycle to increasing amounts of greenhouse gases and aerosols. *Clim. Dyn.*, **20**, 45–68.

Douville, H., 2003: Assessing the influence of soil moisture on seasonal climate variability in AGCMs. *J. Hydrometeor.*, **4** (6), 1044–1066.

Entekhabi, D., I. Rodriguez-Iturbe, and F. Castelli, 1996: Mutual interaction of soil moisture state and atmospheric processes. *J. Hydrology*, **184**, 3–17.

Findell, K.L., and E.A.B. Eltahir, 1997: An analysis of the soil moisture-rainfall feedback based on direct observations from Illinois *Water Resources Res.*, **33**, 725–735.

Findell, K.L., and E.A.B. Eltahir, 1999: Analysis of the pathways relating soil moisture and subsequent rainfall in Illinois. *J. Geophys. Res.- Atmos.*, **104**, 31565–31574.

Gochis, D.J., W.J.A. Shuttleworth, and Z.L. Yang, 2002: Sensitivity of the modeled North American monsoon regional climate to convective parameterization. *Mon. Wea. Rev.*, **130**, 1282–1298.

Guo, Z., and the GLACE Team, 2006: GLACE: The Global Land-Atmosphere Coupling Experiment. 2. Analysis., *J. Hydrometeor.*, **7** (4), 611–625.

Hong, S.-Y., and E. Kalnay, 2000: Role of sea surface temperature and soil-moisture feedback in the 1998 Oklahoma-Texas drought. *Nature*, **408**, doi:10.1038.35048548, 842–844.

IPCC, 2007: Climate Change 2007: The Physical Science Basis. Contribution of Working Group I to the Fourth Assessment Report of the Intergovernmental Panel on Climate Change. Solomon, S., D. Qin, M. Manning (eds.).

Johns, T.C., J.M. Gregory, W.J. Ingram, C.E. Johnson, A. Jones, J.A. Lowe, J.F.B. Mitchell, D.L. Roberts, D.M.H. Sexton, D.S. Stevenson, S.F.B. Tett, and M.J. Woodage, 2003: Anthropogenic climate change for 1860 to 2100 simulated with the HadCM3 model under updated emissions scenarios. *Clim. Dyn.*, **20**, 583–612.

Knutson, T.R., and R.E. Tuleya, 2004: Impact of CO2-induced warming on simulated hurricane intensity and precipitation: Sensitivity to the choice of climate model and convective parameterization. *J. Climate*, **17**, 3477–3495.

Koster, R.D., M.J. Suarez, and M. Heiser, 2000: Variance and predictability of precipitation at seasonal-to-interannual timescales. *J. Hydrometeor.*, **1**, 26–46.

Koster, R.D., P.A. Dirmeyer, P.C.D. Milly, and G.L. Russell, 2001: Comparing GCM-generated land surface water budgets using a simple common framework. In *Land Surface Hydrology, Meteorology, and Climate: Observations and Modeling*, V. Lakshimi, J. Albertson, and J. Schaake, Editors, American Geophysical Union, Washington, D.C., 95–105.

Koster, R.D., P.A. Dirmeyer, A.N. Hahmann, R. Ijpelaar, L. Tyahla, P. Cox, and M.J. Suarez, 2002: Comparing the degree of land-atmosphere interaction in four atmospheric general circulation models. *J. Hydrometeor.*, **3**, 363–375.

Koster, R.D., M.J. Suarez, R.W. Higgins, and H.M. Van den Dool, 2003: Observational evidence that soil moisture variations affect precipitation. *Geophys. Res. Lett.*, **30**, doi:10.1029/2002GL016571.

Koster, R.D., and the GLACE Team, 2004: Regions of strong coupling between soil moisture and precipitation. *Science*, **305**, 1138–1140.

Koster, R.D., and M.J. Suarez, 2004: Suggestions in the observational record of land-atmosphere feedback operating at seasonal time scales. *J. Hydrometeor.*, **5**, 567–572.

Lin, J.W.-B., J.D. Neelin, and N. Zeng, 2000: Maintenance of tropical intraseasonal variability: Impact of evaporation-wind feedback and midlatitude storms. *J. Atmos. Sci.*, **57**, 2793–2823.

Lintner, B.R., and J.C.H. Chiang, 2005: Reorganization of tropical climate during El Niño: a weak temperature gradient approach. *J. Climate*, **18** (24), doi:10.1175/JCLI3580.1, 5312–5329.

Lintner, B.R., and J.D. Neelin, 2007: A prototype for convective margin shifts. *Geophys. Res. Lett.*, **34** (5), doi:10.1029/2006GL027305, L05812.

Maloney, E.D., and D.L. Hartmann, 2001: The sensitivity of intraseasonal variability in the NCAR CCM3 to changes in convective parameterization. *J. Climate*, **14**, 2015–2034.

Moore, N., and S. Rojstaczer, 2002: Irrigation's influence on precipitation: Texas High Plains, USA. *Geophys. Res. Lett.*, **29**, Art. No. 1755.

Neelin, J.D., and N. Zeng, 2000: A quasi-equilibrium tropical circulation model—formulation. *J. Atmos. Sci.*, **57**, 1741–1766.

Neelin, J.D., and H. Su, 2005: Moist teleconnection mechanisms for the tropical South American and Atlantic sector. *J. Climate*, **18**, 3928–3950.

Neelin, J.D., M. Munnich, H. Su, J.E. Meyerson, and C.E. Holloway, 2006: Tropical drying trends in global warming models and observations. *Proc. Nat. Acd. Sci.*, **103**, 6110–6115.

Notaro, M., 2008: Statistical identification of global hot spots in soil moisture feedbacks among IPCC AR4 models. *J. Geophys. Res.*, , **113**, D09101.

Pal, J.S., and E.A.B. Eltahir, 2001: Pathways relating soil moisture conditions to future summer rainfall within a model of the land-atmosphere system. *J. Climate*, **14**, 1227–1242.

Pal, J.S., and E.A.B. Eltahir, 2003: A feedback mechanism between soil-moisture distribution and storm tracks. *Quart. J. Roy. Meteor. Soc.*, **129**, 2279–2297 Part A.

Schär, C., D. Luthi, and U. Beyerle, 1999: The soil-precipitation feedback: A process study with a regional climate model. *J. Climate*, **12**, 729–741.

Shukla, J., and Y. Mintz, 1982: The influence of land-surface evapotranspiration on Earth's climate. *Science*, **215**, 1498–1501.

Sobel, A.H., and C.S. Bretherton, 2000: Modeling tropical precipitation in a single column. *J. Climate*, **13**, 4378–4392.

Soden, B.J., and I.M. Held, 2006: Robust responses of the hydrological cycle to global warming. *J. Climate*, **19**, 5686–5699.

Steiner, A.L., J.S. Pal, S.A. Rauscher, J.L. Bell, N.S. Diffenbaugh, L.C. Sloan, and F. Giorgi, 2008: Land surface coupling in regional climate simulations of the West African monsoon. *Clim Dyn.* **in preparation**.

Su, H., J.D. Neelin, and J.E. Meyerson, 2003: Sensitivity of tropical tropospheric temperature to sea surface temperature forcing. *J. Climate*, **16**, 1283–1301.

Stidd, C.K., 1975: Irrigation increases rainfall? *Science*, **188**, 279–281.

Taylor, C.M., F. Said, and T. Lebel, 1997: Interactions between the land surface and mesoscale rainfall variability during HAPEX-Sahel. *Mon. Wea. Rev.*, **125**, 2211–2227.

Taylor, C.M., and T. Lebel, 1998: Observational evidence of persistent convective-scale rainfall patterns. *Mon. Wea. Rev.*, **126**, 1597–1607.

Taylor, C.M., R.J. Ellis, D.J. Parker, R.R. Burton, and C.D. Thorncraft, 2003: Linking boundary layer variability with convection: A case-study from JET2000. *Quart. J. Roy. Meteor. Soc.*, **129**, 2233–2253.

Vinnikov, K.Y., A. Robock, N.A. Speranskaya, and C.A. Schlosser, 1996: Scales of temporal and spatial variability of soil moisture. *J. Geophys. Res.,* **101**, 7163–7174.

Wang, H., and R. Fu, 2002: Cross-equatorial flow and seasonal cycle of precipitation over South America. *J. Climate,* **15**, 1591–1608.

Williams, K.D., C.A. Senior, and J.F.B. Mitchell, 2001: Transient climate change in the Hadley Centre models: The role of physical processes. *J. Climate,* **14**, 2659–2674.

Wu, W., R.E. Dickinson, H. Wang, Y. Liu, and M. Shaikh, 2007: Covariabilities of spring soil moisture and summertime United States precipitation in a climate simulation. *Int. J. Climatol.*, **27**, 429–438.

Xue, Y., and J. Shukla, 1993: The influence of land-surface properties on Sahel climate. Part 1: Desertification. *J. Climate,* **6**, 2232–2245.

Zeng, N., J.D. Neelin, K.M. Lau, and C.J. Tucker, 1999: Enhancement of interdecadal climate variability in the Sahel by vegetation interaction. *Science*, **286**, 1537–1540.

Zeng, N., J.D. Neelin, and C. Chou, 2000: A quasi-equilibrium tropical circulation model–Implementation and simulation. *J. Atmos. Sci.,*, **57**, 1767–1796.

Zhang, G.J., and N.A. McFarlane, 1995: Sensitivity of climate simulations to the parameterization of cumulus convection in the Canadian Climate Center general-circulation model. *Atmos.-Ocean*, **33**, 407-446.

Zheng, X., and E.A.B. Eltahir, 1998: A soil moisture-rainfall feedback mechanism. 2. Experiments with a simple numerical model. *Water Resource Res.*, **34**, 777–785.

Table and Figure Captions

TABLE 1: Breakdown of σ_E^2 for the standard and fixed β simulations. Values tabulated are in units of mm^2 day^{-2}.

FIGURE 1: 3-month seasonal average standard deviations (σ) of QTCM1 control run precipitation (a) and ratio of control run to fixed β σ (b). The shaded contours in (a) are in units of mm day^{-1}, while those in (b) are nondimensional. In (b), only those regions where the ratio exceeds 1 are shaded. Line contours denote seasonal mean precipitation (in mm day^{-1}).

FIGURE 2: (a) Dependence of x_c^E (equation 12) on top-of-the-atmosphere radiation (R_{toa}) for different values of evaporation (E). The curves plotted (in units of 1000 km relative to the inflow point) correspond to $E =$ 0, 10, and 20 W m^{-2} (red, green, and blue respectively). Note that a value of u_q of 1 m s^{-1} has been assumed. Dashed vertical lines correspond to asymptotes of x_c^E, which occur at $R_{toa} = -M_{qp}q_c(T)M_s^{-1}E$. (b) Logarithmic derivative of x_c^E with respect to E for R_{toa} of 10, 30, 50, and 70 W m^{-2} (black, red, green, and blue, respectively). Values given are in units of percent per W m^{-2}.

FIGURE 3: Time-mean precipitation profiles (solid lines) as simulated by the idealized "tropical strip" configuration of QTCM1 (see text in Section 4a for a detailed description): standard perturbation case with stochastic, Gaussian barotropic windfield perturbations of 10 days duration imposed in QTCM1's horizontal moisture advection scheme (red); fixed β case, i.e., the evaporation efficiency factor β prescribed to a time mean value estimated from the standard case (blue); and no wetness memory, i.e., the total evaporation based on a functional fit of the relationship between E and P obtained from the standard case (green). The dashed lines are standard deviations of the precipitation profiles for the standard (red), fixed β (blue), and no wetness memory (green) cases. The distance along the horizontal axis has been normalized by the x_c obtained in the absence of perturbation forcing, with a value of 0 denoting the land-ocean interface and a value of 1 denoting the no perturbation x_c.

FIGURE 4: Relationships of convective margin locations x_c to applied windfield perturbations δu_0 using the QTCM1 tropical strip configuration for (a) R_{toa} $\approx$70 W m^{-2} and (b) R_{toa} $\approx$26 W m^{-2}. The data points shown consist of bin-averages according to δu_0 values with bin widths defined by percentiles of the normal distribution for the standard perturbation (red), "fixed β" (blue), and "no wetness memory" (green) experiments. The x_c values represent the margin location on the final day of each 10-day interval of perturbation, normalized by the margin x_c obtained in the absence of perturbation forcing. The error bars correspond to the standard error, $se_i = \sigma_i/\sqrt{N}_i$, of each bin, where σ_i is the standard deviation of each bin average and N_i is the number of data points per bin. Also shown in each panel are the steady-state analytic solutions estimated from equations (13) (no evaporation; black lines) and (15) (residual evaporation; gray lines).

FIGURE 5: Precipitation variance budgets for the STND (a) and fixed β (b) idealized QTCM1 simulations. Shown are the variances of precipitation (black), component variances associated with moisture convergence (orange), moisture advection (red), and evaporation (green), and covariances of moisture convergence-moisture advection (dark blue), moisture convergence-evaporation (light blue), and moisture advection-evaporation (purple). Panel (c) illustrates the decomposition of $\sigma^2_{M_{qp}q\nabla\cdot v}$ (black) into variances associated with R_{toa} (green) and $u_q\partial_x q$ (red) and the covariance of R_{toa}-$u_q\partial_x q$ (blue) for the STND simulation (solid lines) and fixed β simulation (dashed lines).

FIGURE 6: (a) Variance differences between the STND and fixed β cases. Shown are the differences for σ_P^2 (black) and σ_E^2 (gray), , in units of mm^2 day^{-2}, plotted against the mean P (in mm day^{-1}). Also shown is σ_β^2 (dashed line; relative to the dimensionless axis on the right-hand side). (b), σ_P^2 (black) and σ_E^2 (gray) for $\tau_c =$ 0.5 hrs (squares) and $\tau_c = 5$ hrs (triangles).

FIGURE 7: Zonal location of the convective margin over Northeastern South America at 5°S for 5-day (pentadal) averages. The black (gray) line illustrates the location of the 2 mm day^{-1} precipitation contour for a soil moisture holding capacity of 150 (15) mm. (Note that the range of pentads shown covers late May through December.) For comparison, the location of the 2 mm day^{-1} precipitation contour estimated from the CMAP precipitation data (squares, for 1979-2002) is also included. The shaded contours illustrate positive values of soil wetness difference of the 150 mm and 15 mm simulations.

FIGURE 8: Zonal cross-sections of precipitation (solid lines), evaporation (dashed lines), and soil wetness (squares) for the standard QTCM1 simulation (black) and the simulation with soil moisture explicitly removed when P = 0 (gray). Results shown are averaged over pentads 50-54. The dashed vertical lines and light brown arrow indicate the region for which soil moisture is zeroed out in this averaging period. The dark brown shading highlights that the precipitation field is altered downstream of where the soil soil moisture is perturbed.

Term	Standard	Fixed β
$\overline{E}_p^2 \sigma_\beta^2$	26.9	0
$\overline{\beta}^2 \sigma_{E_p}^2$	9.6	0.2
$2\overline{\beta E}_p cov(\beta, E_p)$	-23.1	0
$\mathcal{R}_{Evap}$	-8.9	0

TABLE 1: Breakdown of σ_E^2 for the standard and fixed β simulations. Values tabulated are in units of mm^2 day^{-2}.

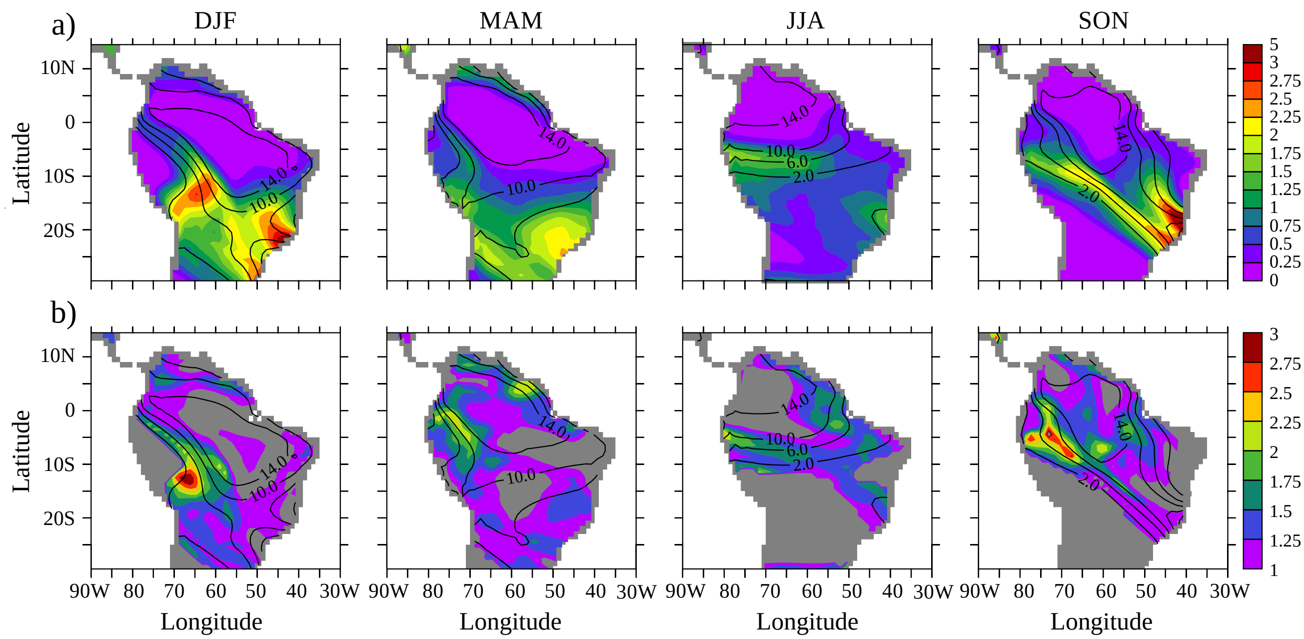

FIGURE 1: 3-month seasonal average standard deviations (σ) of QTCM1 control run precipitation (a) and ratio of control run to fixed β σ (b). The shaded contours in (a) are in units of mm day^{-1}, while those in (b) are nondimensional. In (b), only those regions where the ratio exceeds 1 are shaded. Line contours denote seasonal mean precipitation (in mm day^{-1}).

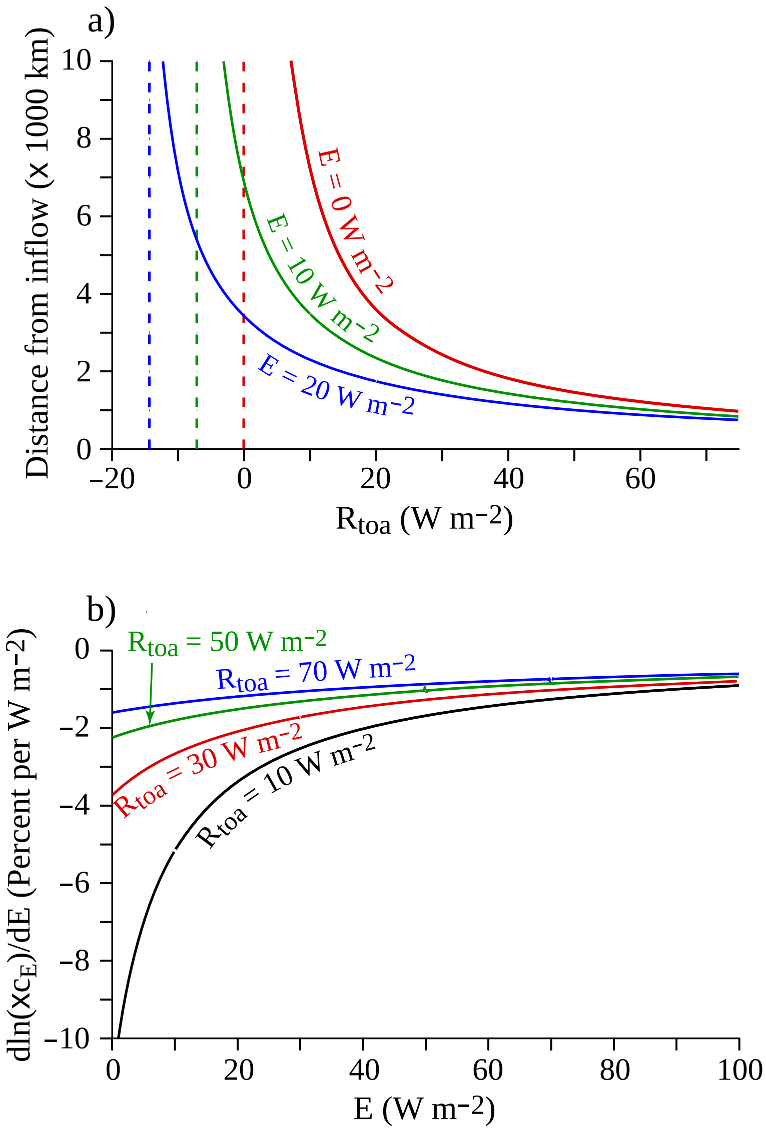

FIGURE 2: (a) Dependence of x_c^E (equation 12) on top-of-the-atmosphere radiation (R_{toa}) for different values of evaporation (E). The curves plotted (in units of 1000 km relative to the inflow point) correspond to $E = 0$, 10, and 20 W m^{-2} (red, green, and blue respectively). Note that a value of u_q of 1 m s^{-1} has been assumed. Dashed vertical lines correspond to asymptotes of x_c^E, which occur at $R_{toa} = -M_{qp}q_c(T)M_s^{-1}E$. (b) Logarithmic derivative of x_c^E with respect to E for R_{toa} of 10, 30, 50, and 70 W m^{-2} (black, red, green, and blue, respectively). Values given are in units of percent per W m^{-2}.

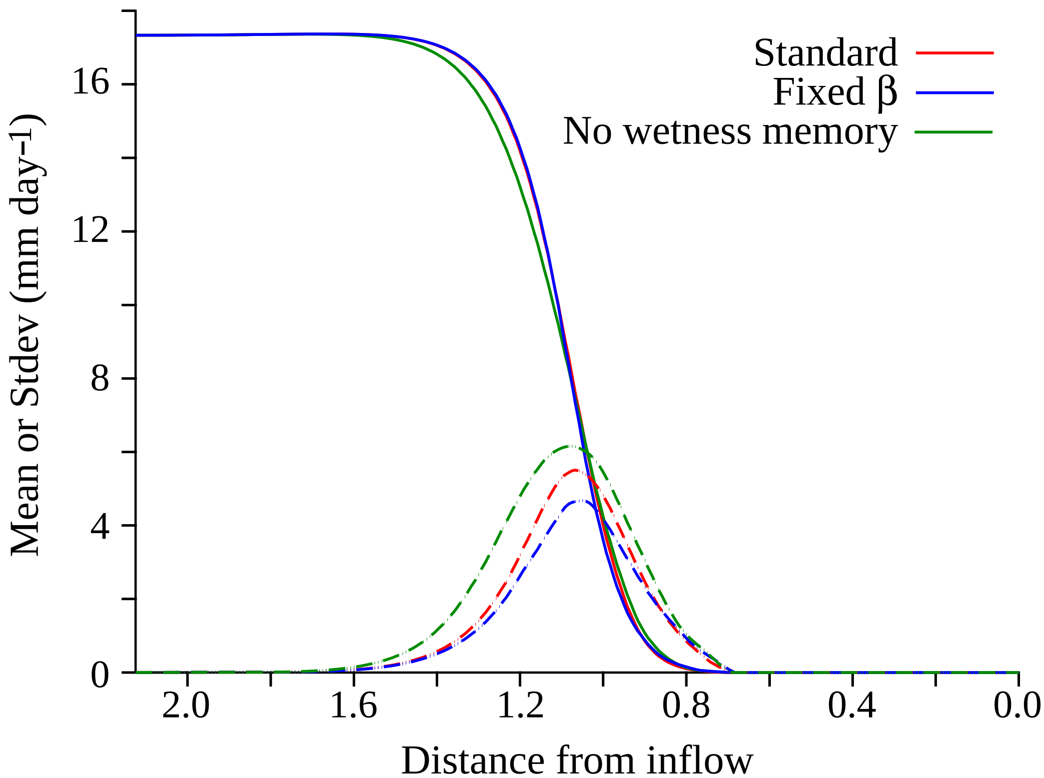

FIGURE 3: Time-mean precipitation profiles (solid lines) as simulated by the idealized "tropical strip" configuration of QTCM1 (see text in Section 4a for a detailed description): standard perturbation case with stochastic, Gaussian barotropic windfield perturbations of 10 days duration imposed in QTCM1's horizontal moisture advection scheme (red); fixed β case, i.e., the evaporation efficiency factor β prescribed to a time mean value estimated from the standard case (blue); and no wetness memory, i.e., the total evaporation based on a functional fit of the relationship between E and P obtained from the standard case (green). The dashed lines are standard deviations of the precipitation profiles for the standard (red), fixed β (blue), and no wetness memory (green) cases. The distance along the horizontal axis has been normalized by the x_c obtained in the absence of perturbation forcing, with a value of 0 denoting the land-ocean interface and a value of 1 denoting the no perturbation x_c.

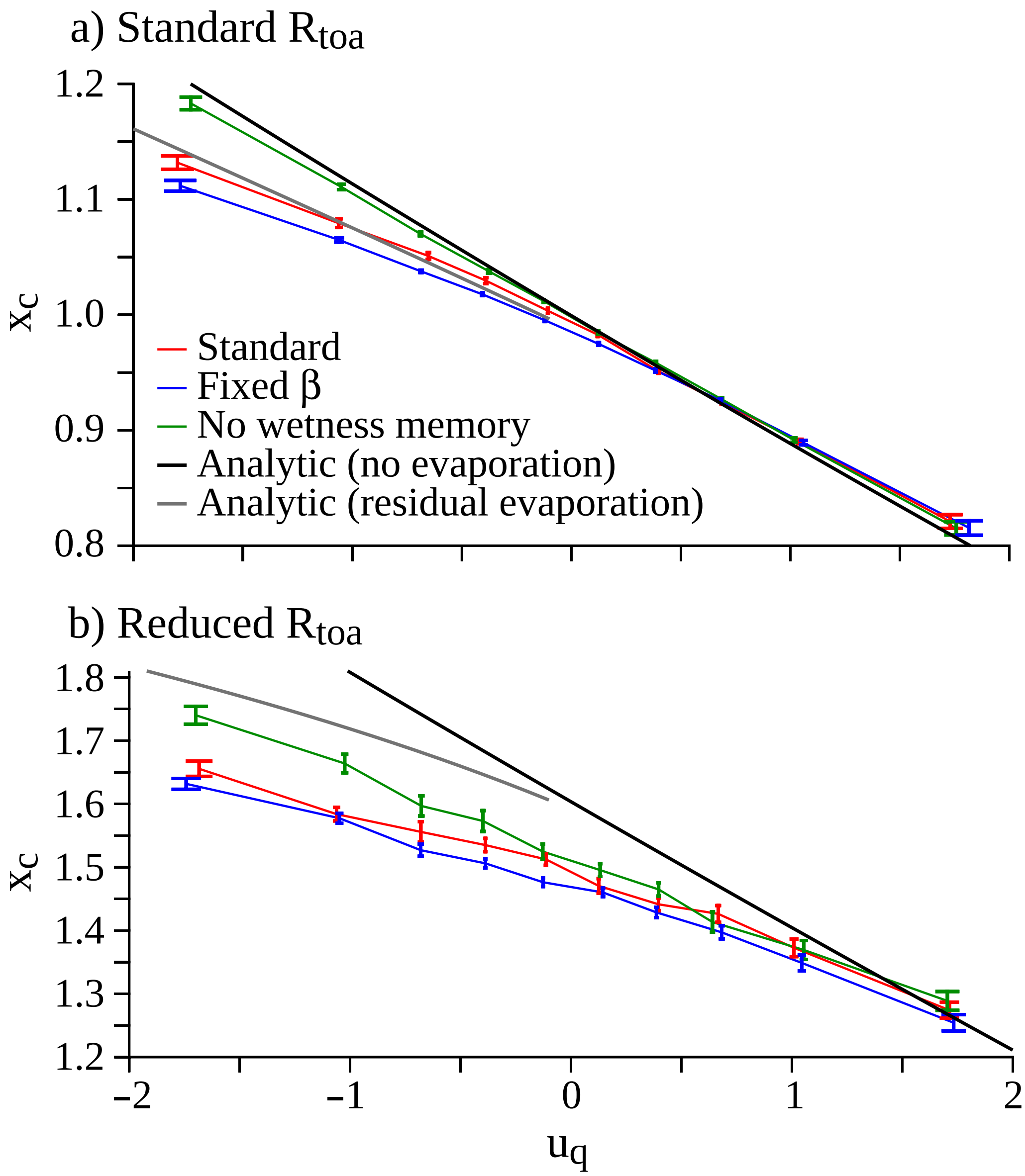

FIGURE 4: Relationships of convective margin locations x_c to applied windfield perturbations δu_0 using the QTCM1 tropical strip configuration for (a) R_{toa} ≈70 W m^{-2} and (b) R_{toa} ≈26 W m^{-2}. The data points shown consist of bin-averages according to δu_0 values with bin widths defined by percentiles of the normal distribution for the standard perturbation (red), "fixed β" (blue), and "no wetness memory" (green) experiments. The x_c values represent the margin location on the final day of each 10-day interval of perturbation, normalized by the margin x_c obtained in the absence of perturbation forcing. The error bars correspond to the standard error, $se_i = \sigma_i/\sqrt{N}_i$, of each bin, where σ_i is the standard deviation of each bin average and N_i is the number of data points per bin. Also shown in each panel are the steady-state analytic solutions estimated from equations (13) (no evaporation; black lines) and (15) (residual evaporation; gray lines).

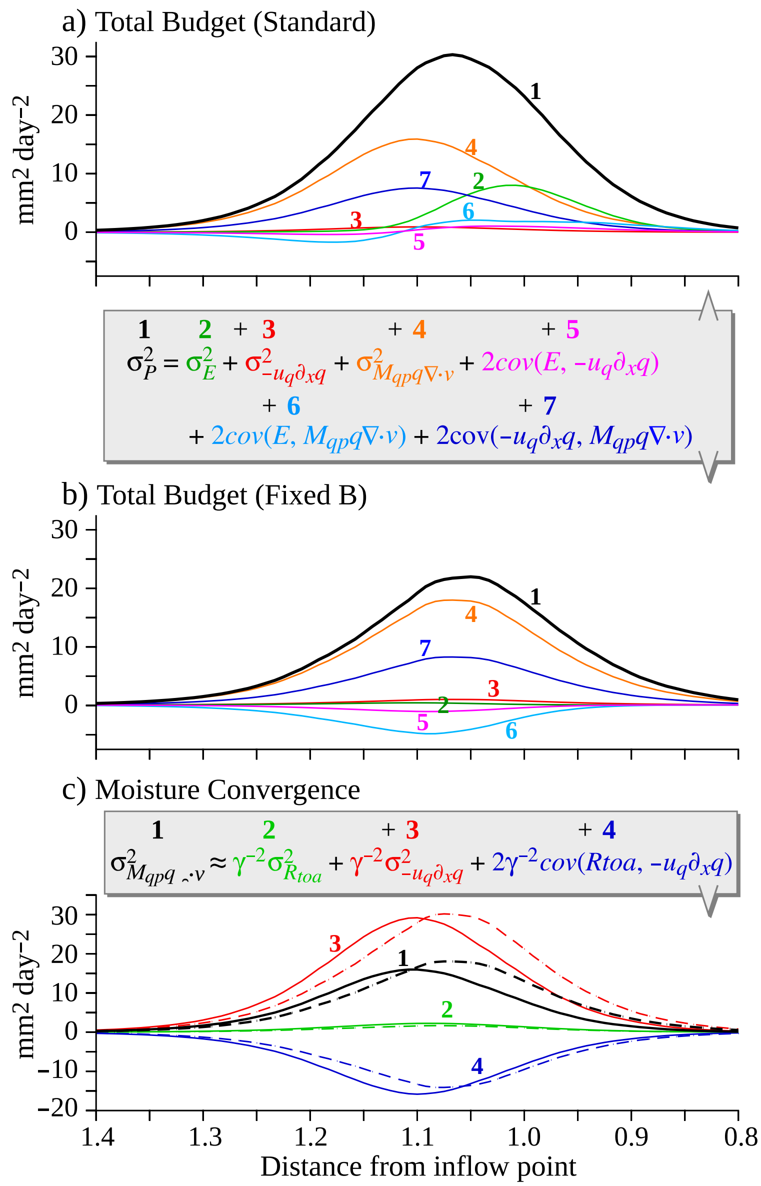

FIGURE 5: Precipitation variance budgets for the STND (a) and fixed β (b) idealized QTCM1 simulations. Shown are the variances of precipitation (black), component variances associated with moisture convergence (orange), moisture advection (red), and evaporation (green), and covariances of moisture convergence-moisture advection (dark blue), moisture convergence-evaporation (light blue), and moisture advection-evaporation (purple). Panel (c) illustrates the decomposition of $\sigma^2_{M_{qp}q\nabla\cdot v}$ (black) into variances associated with R_{toa} (green) and $u_q\partial_x q$ (red) and the covariance of R_{toa}-$u_q\partial_x q$ (blue) for the STND simulation (solid lines) and fixed β simulation (dashed lines).

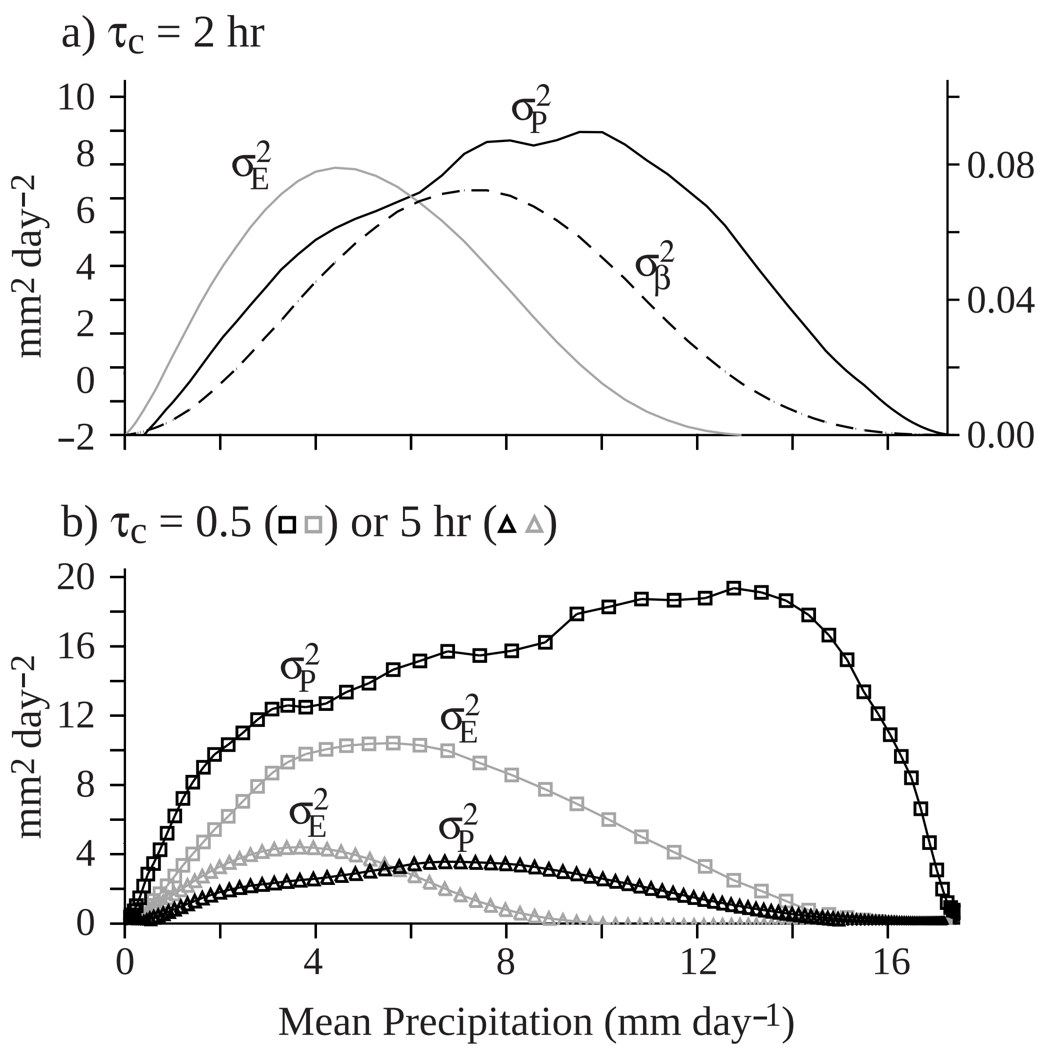

FIGURE 6: (a) Variance differences between the STND and fixed β cases. Shown are the differences for σ_P^2 (black) and σ_E^2 (gray), , in units of mm^2 day^{-2}, plotted against the mean P (in mm day^{-1}). Also shown is σ_β^2 (dashed line; relative to the dimensionless axis on the right-hand side). (b), σ_P^2 (black) and σ_E^2 (gray) for $\tau_c = 0.5$ hrs (squares) and $\tau_c = 5$ hrs (triangles).

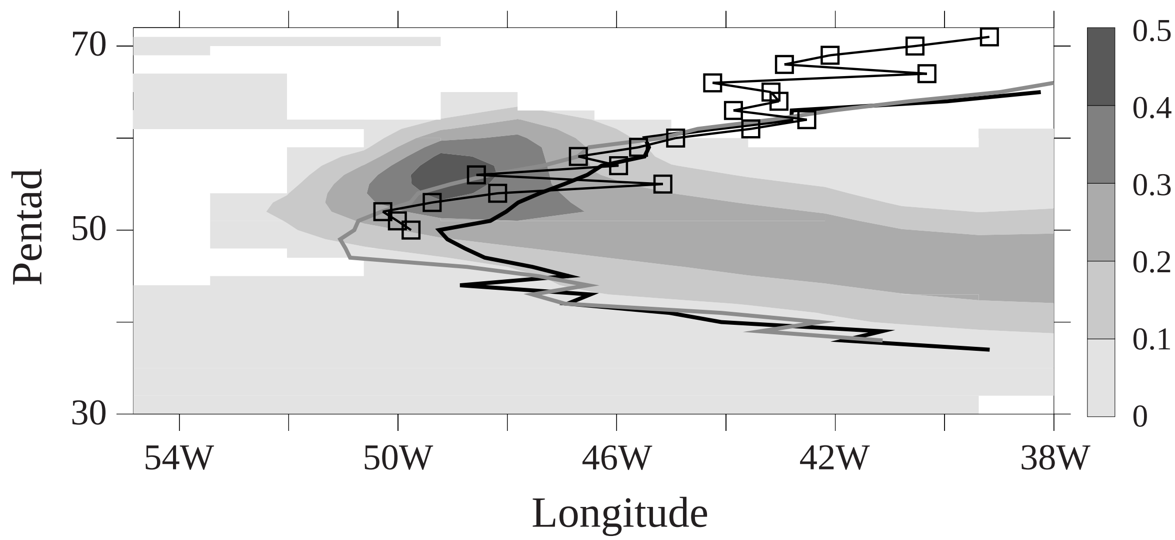

FIGURE 7: Zonal location of the convective margin over Northeastern South America at 5°S for 5-day (pentadal) averages. The black (gray) line illustrates the location of the 2 mm day^{-1} precipitation contour for a soil moisture holding capacity of 150 (15) mm. (Note that the range of pentads shown covers late May through December.) For comparison, the location of the 2 mm day^{-1} precipitation contour estimated from the CMAP precipitation data (squares, for 1979-2002) is also included. The shaded contours illustrate positive values of soil wetness difference of the 150 mm and 15 mm simulations.

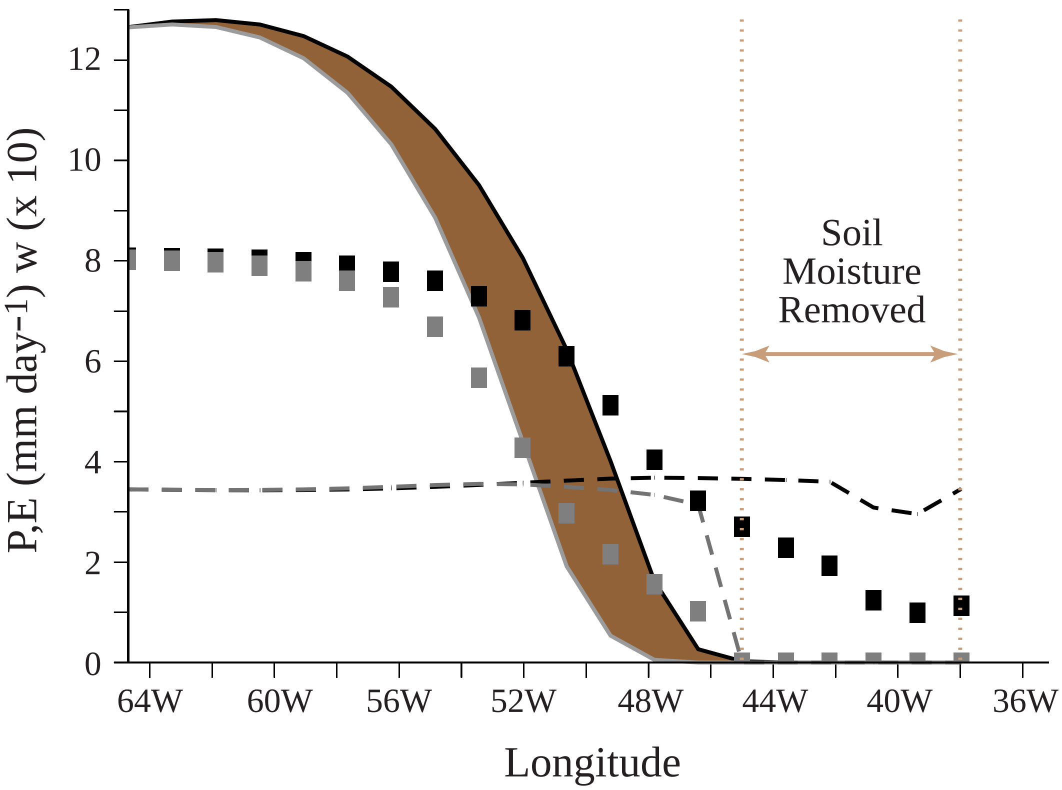

FIGURE 8: Zonal cross-sections of precipitation (solid lines), evaporation (dashed lines), and soil wetness (squares) for the standard QTCM1 simulation (black) and the simulation with soil moisture explicitly removed when $P = 0$ (gray). Results shown are averaged over pentads 50-54. The dashed vertical lines and light brown arrow indicate the region for which soil moisture is zeroed out in this averaging period. The dark brown shading highlights that the precipitation field is altered downstream of where the soil soil moisture is perturbed.